Anal Bioanal Chem (2011) 400:3239–3246
DOI 10.1007/s00216-011-4792-y

ORIGINAL PAPER

Spatial and temporal variations of electron temperatures and densities from EUV-emitting lithium plasmas

R. W. Coons · S. S. Harilal · M. Polek · A. Hassanein

Received: 15 December 2010 / Revised: 7 February 2011 / Accepted: 8 February 2011 / Published online: 26 February 2011
© Springer-Verlag 2011

Abstract Planar slabs of pure Li were irradiated with 1.064 nm, 6 ns Nd:YAG laser pulses. Determination of plasma densities at both the earliest times of plasma formation and near the target surface was performed using Nomarski interferometry. The plasma parameters at later times were evaluated using optical emission spectroscopy. The space- and time-dependent electron densities and temperatures of the plasma were determined from their Stark broadening and the relative intensities of the spectral lines, respectively. The advantages and disadvantages of both of these techniques are evaluated and discussed.

Keyword EUV lithography · Laser-produced plasma · Plasma diagnostics · Emission spectroscopy

Introduction

The optical lithographic processes for semiconductor manufacturing are approaching their theoretical limits [1]. The rate of advancement seen in the semiconductor industry (Moore's Law) is limited by the size of the features that can be etched into substrates, which is limited by the wavelength of the light source used to drive the lithography process. One way to overcome this hurdle is with a new manufacturing technique: extreme ultraviolet lithography [2], which could etch features <32 nm [3]. The leading candidates for the 13.5 nm light sources are laser-produced plasmas (LPP) and discharge-produced plasmas (DPP) [2]. LPP sources have several advantages over DPP sources, such as power scalability, minimal heat loads, and a larger angle of collection. Much research has been conducted on generating LPP from a number of different target materials, including Sn [4], Xe [5], and Li [6]. Many EUV studies focus on Sn exclusively for its high conversion efficiency to 13.5 nm with a 2% bandwidth [7], while ignoring other options such as Li, which has a number of desirable features, such as little heating from out-of-band emissions and less energetic debris [8]. Measurements of the plasma density and temperature are essential to obtain information about plasma expansion dynamics, photon transport, debris characteristics, as well as serving as a benchmark for computer models used to study and optimize these phenomena. Thus, a determination of both the density and temperature of Li LPP throughout their entire evolution is critical for EUV lithography to progress and will be explored in this work.

Plasma densities and temperatures can be evaluated by a number of techniques, including spectroscopy, interferometery, and Langmuir probes [9]. Each diagnostic method has its own limitations, and it is nearly impossible to obtain the basic plasma parameters with a high special and temporal precision during the entire lifetime of the plasma using one diagnostic technique. For example, optical emission spectroscopy (OES) is a versatile tool for estimating plasma parameters at later times; however, this technique fails at earliest times of plume evolution due to strong continuum radiation from the plasma. Moreover, the spatial and temporal mixing of the plasma parameters will affect the accuracy of the measurement. Interferometry techniques are very useful for estimating density at the

Published in the special issue *Laser-Induced Breakdown Spectroscopy* with Guest Editors Jagdish P. Singh, Jose Almirall, Mohamad Sabsabi, and Andrzej Miziolek.

R. W. Coons (✉) · S. S. Harilal · M. Polek · A. Hassanein
School of Nuclear Engineering,
and Center for Materials Under Extreme Environment,
Purdue University,
West Lafayette, IN 47907, USA
e-mail: rwcoons@purdue.edu

earliest time. We used Nomarski interferometery and OES for characterizing the plasma at the earliest and late times, respectively, during its evolution. The accuracy and applicability of each technique will be tested against one another. In addition, the OES studies are performed in a conventional way (1D OES) to generate space- and time-resolved density profiles, along with 2D OES, which measures plasmas throughout their entire expansion in a time-integrated fashion.

Experimental setups and procedures

Schematics of the experimental setups are given in Fig. 1. Plasmas were generated from 1.064 nm, 6 ns FWHM pulses from a Nd:YAG laser, which are attenuated using a combination of a half-wave plate and a polarizing cube. These laser pulses excite planar slabs of pure Li mounted to a servo-motor controlled XYZ translation stage inside of a custom-designed stainless steel high-vacuum chamber. The XYZ stage allows target translation between shots to provide a fresh target surface for each trial, to mitigate effects caused by target drilling and crater formation. The chamber was evacuated using a turbomolecular pump and a base pressure of $\sim 1.3 \times 10^{-4}$ Pa is easily achieved. A 40 mm plano-convex focusing lens was mounted to a micrometer-controlled translation stage outside of the chamber, allowing for the fine tuning of the laser spot size.

Both Nomarski interferometry and OES methods are used to estimate the evolution of plasma density. OES is not a good technique to measure the density at the earliest times and closer distances to the target because of strong interference from the continuum radiation. Similarly, interferometry techniques do not provide densities at later times (<40 ns after plasma formation) and larger distances (>1mm from the target surface) due to minute changes in the refractive properties of plasma. For measuring electron density with the Nomarski interferometer [10], a low-energy (1–5 mJ) 532 nm probe beam is given a 45° polarization by a polarizing cube before passing through the plasma, parallel to the target surface. A short focal length lens (10 cm) was used to relay the plasma image onto the detector plane, and a Wollaston prism was inserted between the relaying lens and detector. The Wollaston prism splits the probe beam into two separate, orthogonally polarized beams, with each being refracted in opposite directions at a very subtle angle (0.6°). A second polarizing cube is used to superimpose the two beams into a single beam of uniform intensity and polarization. This combined beam is focused with a 20 cm focusing lens onto a CCD camera, which images an interference pattern. A 532 nm band-pass filter is placed in front of the camera to filter out the continuum emission, which would obscure the fringes [11], along with neutral density filters to prevent detector saturation.

The refractive index of the plasma plume is a function of its electron density, which rapidly varies throughout the expanding plume. This change in refractive index causes a bending or shifting of the interference fringes, as shown in Fig. 2. These interference patterns are processed with the IDEA software package [12], which utilizes 2D fast-Fourier transform and Abel inversion algorithms to generate phase diagrams. The phase diagram cross-section peaks are

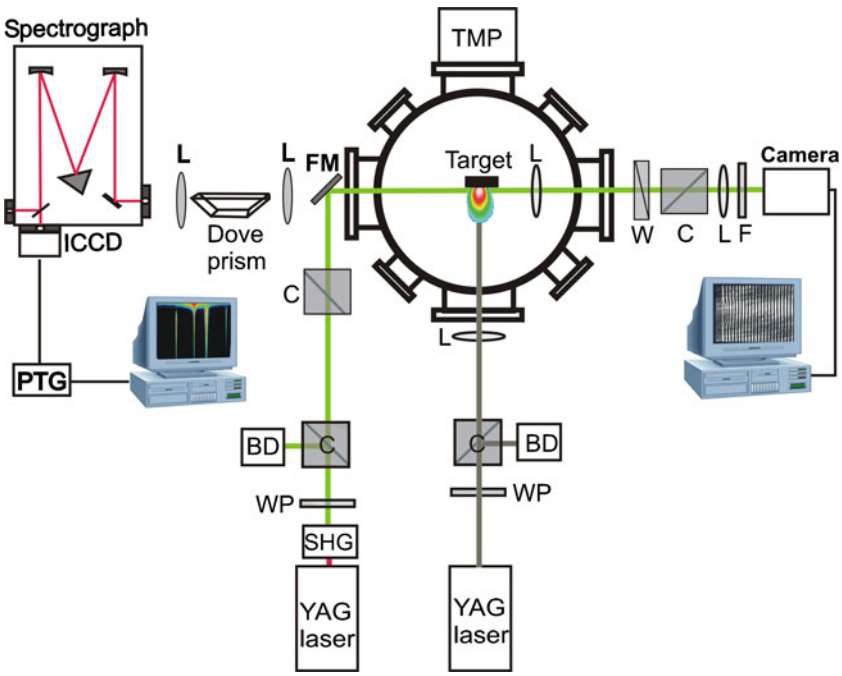

Fig. 1 Schematic of the Nomarski interferometry and 2D OES setup. Optical components include polarizing cubes (*C*), half-wave plates (*WP*), lenses (*L*), the Wallaston prism (*W*), fold mirror (*FM*), and filter (*F*). (*TMP* turbomolecular pump, *PTG* programmable timing generator, *BD* beam dump, *SHG* second harmonic generator)

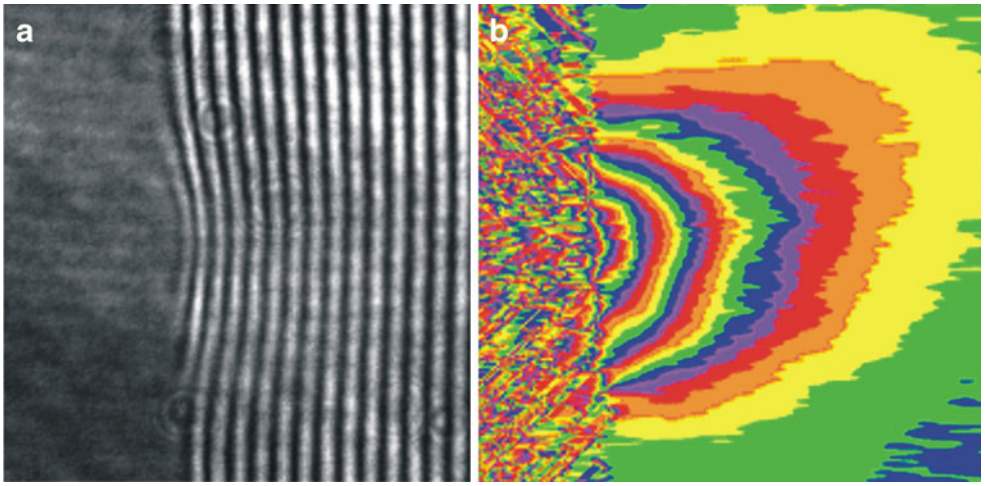

Fig. 2 **a** Interference fringe shift caused by plasma, and **b** IDEA-rendered Abel-inverted phase plot of the interferometry data. All images are for single Li plasma created by 6 ns 1,064 nm laser pulse and at the peak of the pump laser pulse

recorded (Fig. 2b), and the plasma electron density, n_e is obtained plot through the relation:

$$n_e = n_{\text{critical}} \left(\frac{\lambda_{\text{probe}}}{\pi} \right) \left(\frac{\text{Abel peak}}{\text{Scaling factor}} \right) \text{cm}^{-3} \quad (1)$$

where the critical density is given by [13]:

$$n_{\text{critical}} = \left(\frac{10^{21}}{\lambda^2_{\text{probe}}} \right) \text{cm}^{-3} \quad (2)$$

The probe laser wavelength (λ_{probe}) in Eqs. 1 and 2 are in micrometers. The scaling factor is calculated from the CCD pixel size and the measured shadow of a 250 μm wire placed at the laser focus spot.

Electron densities and temperatures were measured using conventional (1D) OES, where the light emitted from the plasma plume was collimated and focused by two 40 mm lenses into a 3 mm high entrance slit of a 0.5 m Czerny–Turner spectrometer. In 1D OES, various plume segments were selected along the plume expansion axis and averaged over line-of-sight. This setup was easily converted to a 2D OES system by inserting a Dove prism between the focusing and collimating lenses. The Dove prism is an optical rotator which turns the plasma plume image 90°, enabling the entire plume image to pass through the spectrometer entrance slit [14]. In the 2D OES setup, the spectrograph entrance slit was changed to a height of 1 cm. Conventional 1D OES generates line-of-sight averaged intensity vs. wavelength plot for a segment in a plasma along the target normal (plume expansion direction). To examine various segments of the plume in the expansion direction, the imaging system must be translated for imaging various locations of the plume at the spectrograph entrance slit. In 2D OES, the ICCD detector is operated in the imaging mode. 2D OES generates an intensity-wavelength plot for each pixel of the detector, at different points in space along the plume expansion direction. A typical 2D spectral image of Li I at 460.3 nm is given in Fig. 3.

The electron density can be quickly determined from intensity vs. wavelength plots of its line emission from its degree of Stark broadening, obtained by fitting a Lorentzian to the transition peak and measuring its full-width at half maximum (FWHM). Then, the electron density of the plasma, n_e, can be calculated from the relation [15]:

$$n_e = \frac{\Delta\lambda_{1/2} 10^{16}}{2W} \quad (3)$$

where $\Delta\lambda_{1/2}$ is the FWHM of the peak (in Ångstrom); and W is the electron impact parameter, which has been tabulated elsewhere [16]. The impact parameters are functions of the electron temperature, but the dependence is negligibly weak [16]. Previous studies indicated that electron densities measured using the available width parameters have ≥20% error [17]. The effects of instrumental broadening were mitigated by minimizing the slit

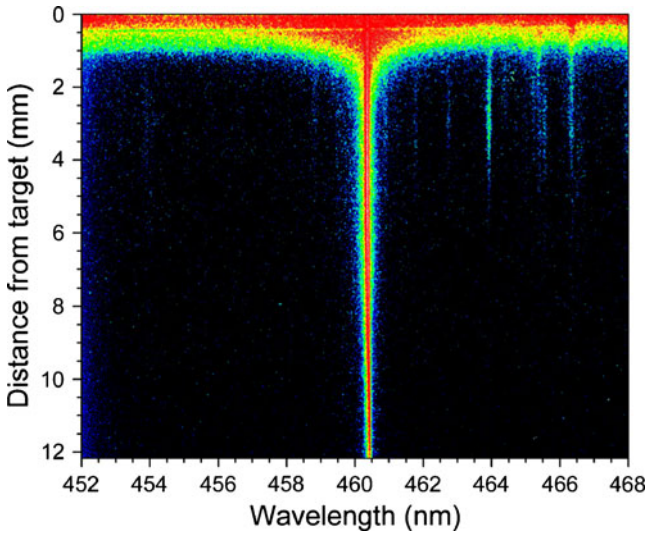

Fig. 3 A typical time-integrated 2D OES plasma profile, recording spectral intensity (indicated by *false-color*) as a function of emitted wavelength and distance from the target. The most prominent line shown is the 460.3 nm line of Li

width of a high-resolution spectrograph to 30 μm. Under these conditions, the maximum resolution available for our spectrograph is ~0.025 nm. The Doppler broadening of Li I was calculated [17] from the debris velocity [8] to be 0.0215 nm, which is very small. Stark broadening was then the dominant broadening mechanism [17]. Stark broadening does not require an assumption of local thermal equilibrium (LTE) to provide a reliable density measurement because the Stark effect is weakly influenced by the electron velocity distribution [17].

Electron temperatures are determined through the Boltzmann plot method, which directly compares the spectral line intensities of LTE plasmas. This is most easily implemented for the case of 2D OES, where the time-integrated spatially resolved electron temperature is determined directly from two spectral lines of a given species through the relation [15]:

$$kT_e = \frac{(E_2 - E_1)}{\ln\left(\frac{I_1\lambda_1 g_2 A_2}{I_2\lambda_2 g_1 A_1}\right)} \quad (4)$$

where T_e is the electron temperature, k is Boltzmann's constant, E is the excitation energy of the transition, I is the relative spectral line intensity, λ is the wavelength of the spectral line, g is the statistical weight of the upper-level transition, and A is the atomic transition probability. The subscript "1" is designated to the transition with the longer wavelength. Evaluating multiple transitions can improve the accuracy of the temperature measurement, by applying the following relation to each transition:

$$I = An\left(\frac{ghc}{Z\lambda}\right)\exp\left(\frac{-E}{kT}\right) \quad (5)$$

where h is Planck's constant, and c is the speed of light in a vacuum. Then, assuming a Maxwellian population distribution, a $\ln(I\lambda/Ag)$ vs. E plot will have a linear slope equal to $-1/kT$ [15]. Temperature measurements were determined from the transitions listed in Table 1. These transitions were chosen because they were the most relatively intense lines within the spectral window of our detector, as well as having parameters available from a spectroscopic database. Likewise, the electron density measurements are determined from OES measurements of the Li I $1s^2 2p–1s^2 4d$ line at 460.29 nm, which has a documented Stark width of 0.149 nm at 10^4K and also lies in the region of best spectral response for our detector. In addition, several lines were used in the temperature determinations that were found to be free of self-absorption, which can be detected with 2D OES by the appearance of a triangular void in the initial continuum emission [18].

Results

Nomarski interferometry

Nomarski interferometry is capable of measuring plasma densities at the earliest times of their formation, ignoring any deleterious effects of the broadband continuum emission. However, Nomarski interferometry is limited by the degree of interference fringe shifting and bending, which becomes less pronounced as the plasma expands, due to the refractive index gradients. Because of this, electron densities can only be recorded at distances <1 mm from the target surface with this technique.

The spatial changes in electron density at various times after the peak of the pump laser pulse are given in Fig. 4. A laser power density of 2.8×10^{11} W/cm^2 is used for this measurement. At the peak of the laser pulse, the quality of the interference fringes will be affected by rapid changes in refractive index. However, at times >10 ns after the peak of the laser pulse, the refractive index gradients are not very rapid, and it is possible to measure the density closest distances to the target surface. The measured densities peak at ~10^{19} cm^{-3} and decays to ~5×10^{17} cm^{-3} within 0.8 mm. It should be remembered that, in LPP, the plasma will be formed by the leading edge of the laser pulse, and the remaining photons will be used for reheating the plasma. The peak density has been found to decrease with time after the peak of the pump laser and with increasing distance from the target surface. The Nomarski density plots have been fitted with 10% error bars to account for fluctuating laser intensity, but the uncertainty may be greater for the reasons discussed above.

Table 1 Parameters of the atomic and ionic transition lines used in the electron temperature and density measurements of Li plasmas [16, 19–21]

Ionization stage	Emission wavelength, λ (nm)	Configuration	Transition probability, A_{ki} (s^{-1})	Statistical weight, g_k	Upper-level energy, E_k (eV)
Li I	413.26	$1s^2 2p–1s^2 5d$	1.06×10^7	6	4.85
Li II	432.54	$1s3p–1s4d$	1.08×10^8	7	72.23
Li I	460.29	$1s^2 2p–1s^2 4d$	2.30×10^7	6	4.54
Li II	548.36	1s2s–1s2p	2.27×10^7	1	61.28
Li I	670.79	$1s^2 2s–1s^2 2p$	3.72×10^7	4	1.85

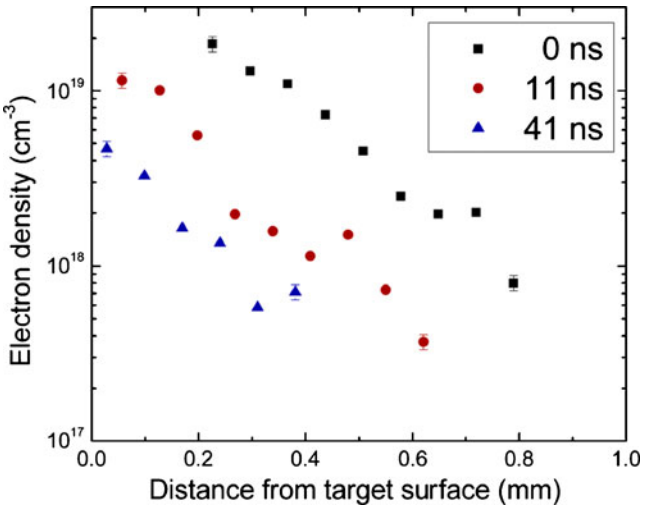

Fig. 4 Electron density vs. distance plots for a spectrally integrated Li LPPs, with varying delay times. The data has been fitted with 10% error bars to account for fluctuating laser intensity, but this may be greater due to additional uncertainties regarding the time of plasma formation

1D OES results

Interferometry provided a measurement of the electron density at the earliest times, and distances very near to the target surface. We performed OES for extending the density measurements at later times and farther distances. Spatially and time-integrated electron densities of laser-produced plasmas were also evaluated through 1D OES, a simple, proven, and common method of plasma analysis which records spectra over the line-of-sight of the detector, perpendicular to the direction of plasma expansion [20, 22]. The spatially resolved electron density, as seen in Fig. 5a, was obtained by translating the focusing lens along the direction of propagation. An integration time of 1 μs is used for this measurement. The spatially resolved density shows the expected exponentially decreasing trend [22]. However, the measured density values at closer distances are more than one order less compared with the density measurement using interferometry. The large discrepancy in the measured values using two different techniques are due to large integration time (1 μs) and spatial averaging in the radiation direction (line-of-sight equivalent to slit height 3 mm) used in the OES measurement. Both 1D and 2D OES density measurements are subject to a minimum of 22.4% error due to inaccuracies in the Stark broadening parameters and fluctuations in the laser intensity.

To understand the detailed aspects of laser-beam interaction with the target material and recombination processes following the laser ablation, time-resolved studies of the emission spectra from the plasma offer the most convenient approach. The time-resolved density is recorded by translating the focusing lens to a fixed point and using

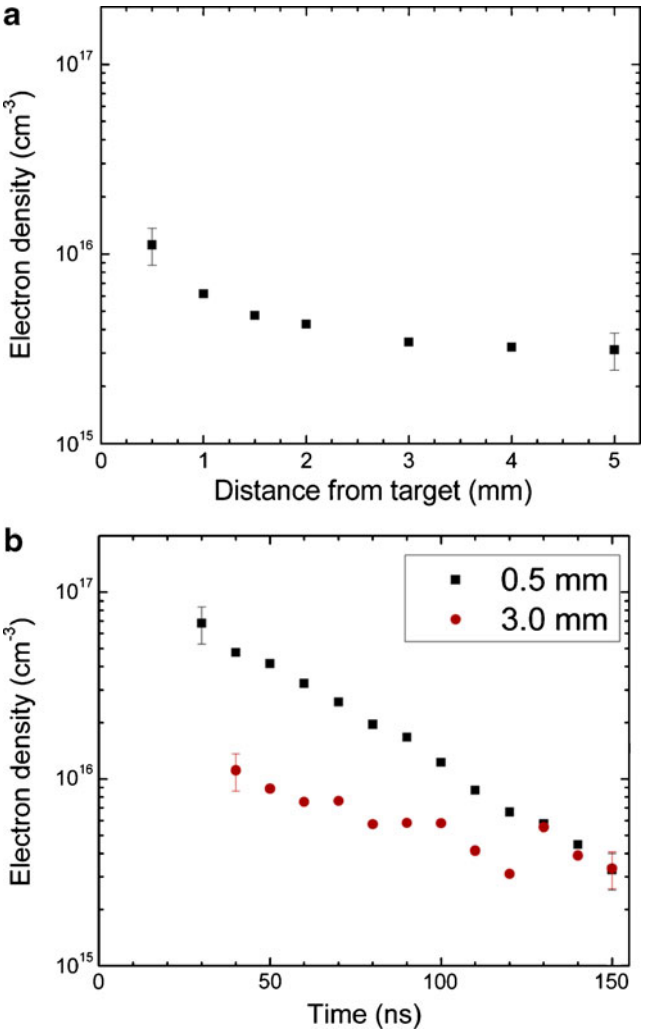

Fig. 5 Electron density of lithium plasma, obtained from measurements of the Li I 460.3 nm line using 1D OES in **a** space-resolved manner with a 1 μm exposure time, and in **b** a time-resolved fashion. There is at least a 22.4% error due to inaccuracies in the Stark broadening parameters and fluctuating laser intensity

the PTG to trigger the ICCD camera to incrementally increase the camera triggering time by 10 ns, as shown in Fig. 5b. The continuum is too strong to obtain information within the first 30–40 ns of plasma formation, but, at later times, the line emission dominates over continuum emission. The time-resolved density appears to have a space-dependence for the first ~125 ns of plasma lifetime, after which the plasma degrades into a cloud of uniform (but time-dependent) density. The time-resolved peak density at a specific point in the plasma is found to be substantially higher especially at short distances from the target surfaces. It indicates that a very high space and time precision is absolutely necessary for obtaining accurate values of plasma parameters.

Because Li is a few-electron system (Z=3), the number of transitions in the visible regime is very limited

[8]. We used the 1s2s–1s2p (^{3}S–^{3}P°) transition of Li II at 548.3 nm and the 1s3p–1s4d (^{3}P–^{3}D) transition of Li II at 432.5 nm, for temperature measurement, as these transitions exhibit a significant excitation energy difference (~11 eV). The estimated time-integrated space-dependence of plasma is given in Fig. 6. The 1D-derived temperature measurement agrees with previously reported values [20]. However, the plasmas generated in the present studies are emitting strongly in the EUV region [8], and hence, the initial temperatures may approach>20 eV during the laser pulse. These measurements show the plasma parameters, both temperature and density, drop rapidly (in time and space) and possess large gradients at the earliest times and shorter distances during plasma evolution. Fluctuating laser intensity creates a 10% uncertainty on all temperature measurements.

2D OES

The plasma properties change with space both in the axial (plume expansion direction) and radial directions. 1D OES measurements are made by averaging over radial distance which is equivalent to slit height (3 mm) used in the present experiment. We imaged the 90°-rotated plasma onto the entrance slit (10 mm height) of the spectrograph with the help of a Dove prism [14]. Using this technique, one can obtain high spatial resolution in the radial direction. The spatial resolution in the axial direction depends on the binning of number of detector pixels.

The 2D OES and the 1D plasma electron densities were recorded under identical experimental conditions. Traditional spectroscopy records a line-of-sight average of plasma plumes, evaluating individual plasmas at a single point, whereas 2D OES records complete plasmas throughout their entire expansion on a one-to-one scale with a spatial integration equal to the spectrometer entrance slit width. We selected various radial distances from the plume expansion axis to evaluate the density gradients (see Fig. 7 inset) along the radial direction. Electron densities were calculated by directly measuring the Stark broadening of 2D OES spectral line cross-sections at a specific point in the plume. The 2D OES trials were conducted in a time-integrated manner, with a 1 μs exposure time and a radial resolution of 30 μm. All plasmas were created with 2.8×10^{11} W/cm^2 laser pulses. The measured density values in the plume expansion (axial) direction using 2D OES at various radial points is given in Fig. 7.

In general, the measured electron plasma density peaked ~7×10^{16} cm^{-3} near the target surface, which decreases exponentially, leveling off at ~3×10^{15} cm^{-3}. The density of Li was found to be an order less than those of Sn [7], which is indicative of a direct Z-dependence on electron density. In the 2D OES setup, translating the imaging lens in the direction of plasma propagation allows for the evaluation of the time-integrated, spatially resolved electron density in different planes throughout the plasma, as illustrated in Fig. 7. There was little difference between the off-axis and centered electron densities ≥1 mm from the target surface. These results suggest that, similar to axial variation of density, large radial gradients observed only at shorter distances from the target surface (<1 mm). Compared with 1D OES, the measured time-integrated peak densities

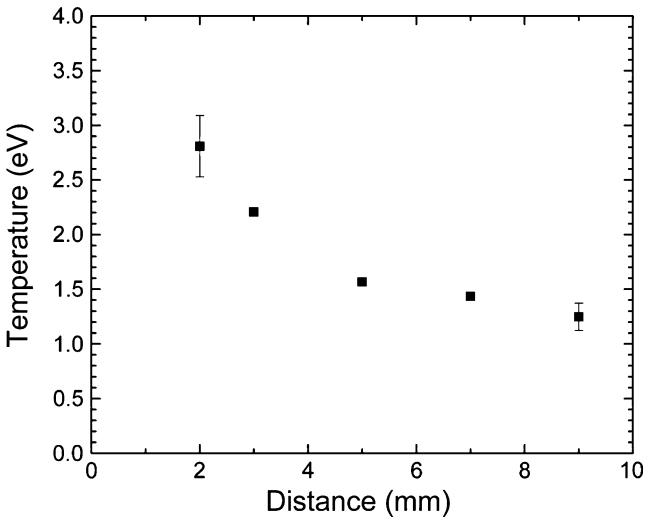

Fig. 6 Spatially resolved plasma electron temperature calculated from the 413.3 nm, 460.3 nm, and 670.8 nm lines of Li I, as determined from 1D OES and the Boltzmann plot method. The spatially resolved was integrated over a 1 μs exposure time. There is a 10 % uncertainty due to fluctuating laser intensity

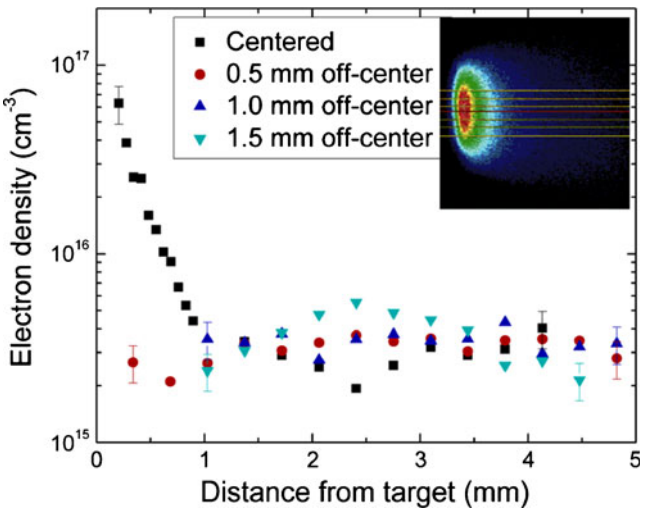

Fig. 7 Off-axis 2D OES density plots of the Li I 460.3 nm line under high vacuum conditions, with a ≥22.4% error due to Stark broadening parameters inaccuracies and fluctuating laser intensity. Typical 2D OES evaluates plasma properties along the central plane of the plasma plume (marked by the *red line* on the *inset*) over 1 μm. Translating the imaging lenses left or right will focus one of the alternate planes (marked by *yellow lines* on the *inset*) into the spectrometer slit

are found to be nearly an order higher for 2D OES trials. However, the discrepancy was noticed only at shorter distances (<1 mm) from the target surface, and it is mainly caused by line-of-sight averaging. At distances ≥1 mm, both techniques agree.

We used 2D OES for a direct intensity comparison based on the Boltzmann plot method to determine the temperature of the plasma with high spatial precision both in the radial and axial direction. The results of this measurement are given in Fig. 8. The maximum temperature of the plasma was found to be ~5.3 eV at 0.36 mm from the target surface. All 2D OES temperature measurements were found to level off at distances >2 mm from the target surface, a level which is consistent with previously reported values [20]. The temperature of Li plasma is significantly higher than that of Sn plasma, which was found to be 1.35 eV at 0.5 mm, and 1.07 eV at 3.0 mm [7], because Li has fewer ionization states than Sn, and thus fewer available options for distributing all of the excitation energy. 2D measurement also showed higher temperature at any specific spatial point in the plasma compared with 1D OES. The temperature values approach similar values at distances ~2 mm. Similar to density, the line-of-sight averaging affect the accuracy of temperature measurement mainly at distances closer to the target. Temperature measurements are again accurate to within 10%, as they are limited by the pulse-to-pulse intensity fluctuations of the laser.

For the temperature measurement, it is essential that plasma be in LTE. The existence of LTE requires that the electron-atom and electron-ion collisional processes occur sufficiently fast and dominate over radiative processes. In a system that is in LTE, particles will have Maxwellian velocity distributions, population levels will be distributed according to Boltzmann's statistics, ionization states will be described by Saha's equation, and the radiation density will obey Planck's law. We confirm the validity of the LTE using the McWhirter criterion [23, 24] which gave a minimum density requirement of 2.90×10^{15} cm^{-3}. The measured density values are higher than the predicted minimum density of the McWhirter criterion; however, the estimated values are very close to the McWhirter criterion, especially >1 mm from the target surface.

The results of 2D OES were merged with the Nomarski interferometry data to create a complete and accurate electron density profile of Li plasmas, which is shown in Fig. 9. It should be remembered that a direct comparison between the peak densities is rather difficult considering the line-of-sight and temporal averaging used in the optical emission spectroscopic studies and the variation of density obtained with high space and time precision in the case of interferometry. However, the combined data showed a very rapid decreasing density trend at short distances (<0.75 mm) and leveling off at distances >2mm.

Conclusions

We investigated the Li plasma properties using time- and space-resolved OES and interferometry. Nomarski interferometry was used to determine electron density at the earliest times of the plasma formation close to the target at different excitation energies and excitation-probe beam delay times. Densities peak at $\sim10^{19}$ cm^{-3}, which decay to $\sim5\times10^{17}$ cm^{-3} within 0.8 mm. These results were merged with 2D OES data to create spatial evolution of electron density of the expanding Li plasma.

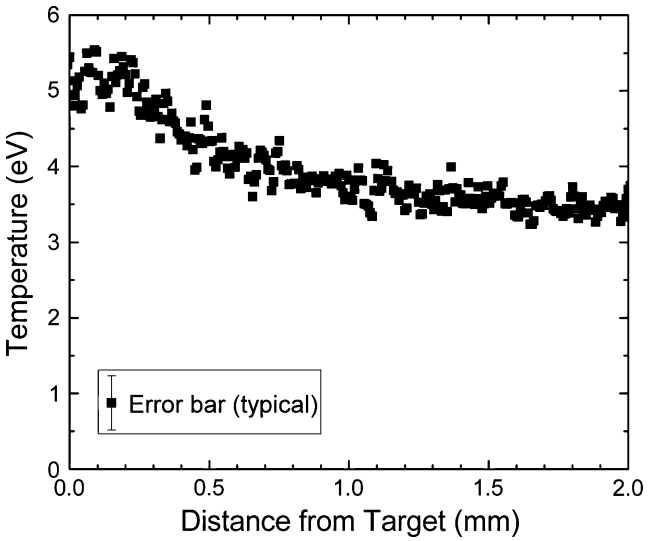

Fig. 8 Electron temperature of Li plasma in high vacuum (~1.3×10^{-4} Pa), calculated from the 432.5 nm and 548.4 nm lines of Li II, as determined by spatially resolved 2D OES, integrated over 1 μs

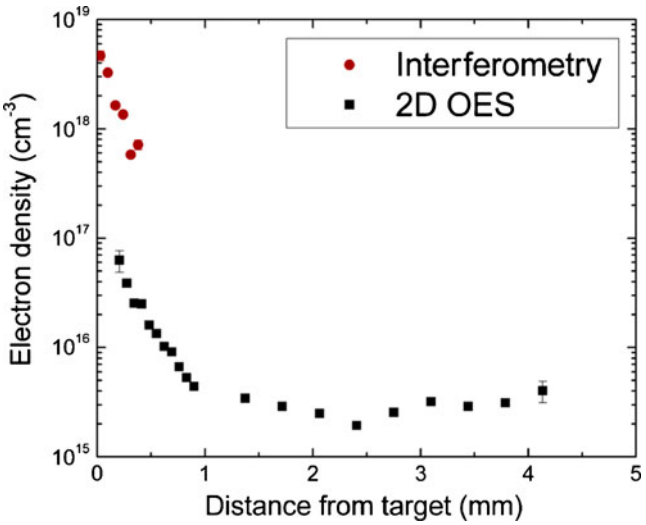

Fig. 9 Complete electron density profile for a Li plasma produced by 100 mJ laser pulse in high-vacuum environment. This is a composite plot created from both the late-time Nomarski interferometry (41 ns delay) data merged with the previous 2D OES data of the Li I 460.3 nm line (1 μs integration time)

Conventional 1D OES was also used to determine spatially and time-resolved electron densities. In addition, 2D OES was used to determine spatially resolved electron densities. The spatially resolved densities showed similar exponentially decreasing trends, but the peak density was an order less than those in the 2D OES trials. However, this peak occurs <1 mm from the target surface, and the discrepancy could be due to line-of-sight averaging in the 1D OES. From the spectroscopy measurements, it has been shown that the plasma density peaks at ~10^{17} cm^{-3} near the target surface and quickly, exponentially decrease to ~3×10^{15} cm^{-3}. Li plasma temperatures were measured with 2D OES and were found to peak at ~5.3 eV at 0.36 mm from the target surface. At distances ≥1 mm, the density values estimated from both 1D and 2D OES are in agreement. The time-resolved density appears to have a spatial dependence which exists for the first ~125 ns of plasma, after which the plasma takes on a single time dependent density that agrees with the 2D OES data.

Acknowledgments The authors would like to thank the Purdue University College of Engineering for their financial support.

References

1. Ito T, Okazaki S (2000) Pushing the limits of lithography. Nature 406(6799):1027–1031
2. Wu B, Kumar A (2007) Extreme ultraviolet lithography: a review. J Vac Sci Technol B 25(6):1743–1761
3. George SA, Silfvast WT, Takenoshita K, Bernath RT, Koay CS, Shimkaveg G, Richardson MC (2007) Comparative extreme ultraviolet emission measurements for lithium and tin laser plasmas. Opt Lett 32(8):997–999
4. Harilal SS, Tillack MS, Tao Y, O'Shay B, Paguio B, Nikroo A (2006) Extreme ultraviolet spectral purity and magnetic ion debris mitigation with low density tin targets. Opt Lett 31(10):1549–1551
5. Bowering N, Martins M, Partlo WN, Fomenkov IV (2004) Extreme ultraviolet emission spectra of highly ionized xenon and their comparison with model calculations. J Appl Phys 95 (1):16–23
6. Higashiguchi T, Kawasaki K, Sasaki W, Kubodera S (2006) Enhancement of extreme ultraviolet emission from a lithium plasma by use of dual laser pulses. Appl Phys Lett 88(16):161502
7. Campos D, Harilal SS, Hassanein A (2010) Laser wavelength effects on ionic and atomic emission from tin plasmas. Appl Phys Lett 96(15):151501
8. Coons RW, Harilal SS, Campos D, Hassanein A (2010) Analysis of atomic and ion debris features of laser-produced Sn and Li plasmas. J Appl Phys 108(6):063306
9. Huddlestone RH (1965) In: Huddlestone RH, Leonard ST (eds) Plasma Diagnostic Techniques. New York, Academic Press
10. Hough P, McLoughlin C, Kelly TJ, Harilal SS, Mosnier JP, Costello JT (2009) Time resolved Nomarski interferometery of laser produced plasma plumes. Appl Surf Sci 255(10):5167–5171
11. Tao Y, Tillack MS, Harilal SS, Sequoia KL, Najmabadi F (2007) Investigation on the interaction of a laser pulse with a preformed Gaussian Sn plume for an extreme ultraviolet lithography source. J Appl Phys 101(2):023305
12. Hipp M, Woisetschlager J, Reiterer P, Neger T (2004) Digital evaluation of interferograms. Measurement 36(1):53–66
13. Jonkers J (2006) High power extreme ultra-violet (EUV) light sources for future lithography. Plasma Sources Sci Technol 15(2): S8–S16
14. Doria D, Kavanagh KD, Costello JT, Luna H (2006) Plasma parametrization by analysis of time-resolved laser plasma image spectra. Meas Sci Technol 17(4):670–674
15. Harilal SS, O'Shay B, Tillack MS, Mathew MV (2005) Spectroscopic characterization of laser-induced tin plasma. J Appl Phys 98(1):013306
16. Griem HR (1974) Spectral line broadening by plasmas. Academic Press, New York
17. Wiese WL (1965) Line Broadening. In: Huddlestone RH, Leonard ST (eds) Plasma diagnostic techniques. Academic Press, New York
18. Siegel J, Epurescu G, Perea A, Gordillo-Vazquez FJ, Gonzalo J, Afonso CN (2004) Temporally and spectrally resolved imaging of laser-induced plasmas. Opt Lett 29(19):2228–2230
19. Ralchenko Y, Kramida, A.E., Reader, J., and NIST ASD Team (2010) NIST Atomic Spectra Database (ver. 4.0.1), [Online]. National Institute of Standards and Technology. http://physics.nist.gov/asd Accessed January 25 2011
20. Bhattacharya D (2000) Plasma dynamics from laser ablated solid lithium. Pramana 55(5–6):823–833
21. Dimitrijevic MS, Sahal-Brechot S (1995) Stark broadening of Li II spectral lines. Phys Scr 54(1):50–55
22. McCormack T, O'Sullivan G (1999) Spatially resolved spectra of resonantly pumped laser produced plasmas of lithium. Rev Sci Instrum 70(6):2674–2680
23. McWhirter RWP (1965) Spectral intensities. In: Huddlestone RH, Leonard ST (eds) Plasma diagnostic techniques. Academic Press, Inc., New York
24. Bekefi G (ed) (1976) Principles of laser plasmas. Wiley, New York